ON THE DIRECTIVITY OF THE PINNAE OF THE RUFOUS HORSESHOE BAT *(RHINOLOPHUS ROUXII)*

Gordon Leonard[1], James A. Flint[1] and Rolf Müller[2]

[1] Department of Electronic and Electrical Engineering, Loughborough University, Ashby Road, Loughborough, Leicestershire, LE11 3TU, UK E-Mail: G.Leonard@lboro.ac.uk

[2] The Maersk Mc-Kinney Moller Institute for Production Technology, University of Southern Denmark, Campusvej 55, DK-5230 Odense M, Denmark E-Mail: rolfm@mip.sdu.dk

ABSTRACT

In this paper the directivity of bat pinnae is considered by analogy with the inverse problem of a radiating aperture. It is shown that previously published measurements of the physical aperture are in some cases coincident with the acoustic aperture. This observation is used to provide a comparison for a full-wave three dimensional numerical simulation of the pinna of the species *Rhinolophus rouxii* (the Rufous Horseshoe bat). The numerical technique incorporated detailed morphological features captured from a computed tomography scan and was based on the Transmission Line Modelling method (TLM). Simulated directivity patterns suggest a gain of 24 dB over the isotropic case, which is in good agreement with measurements.

1. INTRODUCTION

Many species of microbats use sound for navigating around their surroundings, to hunt for food or communication [1]. Sound is projected from the larynx and emitted through the mouth or the nostrils. Ultrasonic emissions then ensonify the target which may be prey, an obstacle, or a landmark. The bat's outer ears (pinnae) direct the reflected sound towards the middle ear, which is followed by mechano-electrical transduction and further processing in the inner ear. Bat pinnae have been examined by a number of researchers in the past, and have been the subject of much experimental work. The complex shape and the vast range of sizes and diversity of geometrical features between species make them a fascinating and challenging area of study.

One motivation for understanding their precise function is the potential to design high performance biomimetic ultrasonic sensory systems for the next generation of mobile robots. It is also intriguing to consider the possibility of applying the shape to antennas for communications systems. A very thorough analysis of the properties of post-mortem ears has been carried out by Obrist *et. al.* [2]. Their analysis has emphasised the wide degree of variability in operating frequency and morphology between species and this is reflected in the differing directional properties measured. They have provided the height and width of the physical aperture for different species, and therefore it is possible to carry out some straightforward calculations. If it is assumed that the aperture is a simple geometrical shape such as a circle or rectangle, then the directivity can be estimated using the analytical expressions inset within Figure 1. In Table 1, the measurements from [2] are reproduced alongside estimates of directivity based on a circular aperture with diameter corresponding with the height, D(H); a circular aperture with diameter corresponding with the width, D(W); and a rectangular aperture with width and height identical to the pinna width and height, D(Rec). The species tabulated are a subset of those covered in [2]

and were selected by virtue of the species being a known transmitter of CF (continuous frequency) signals.

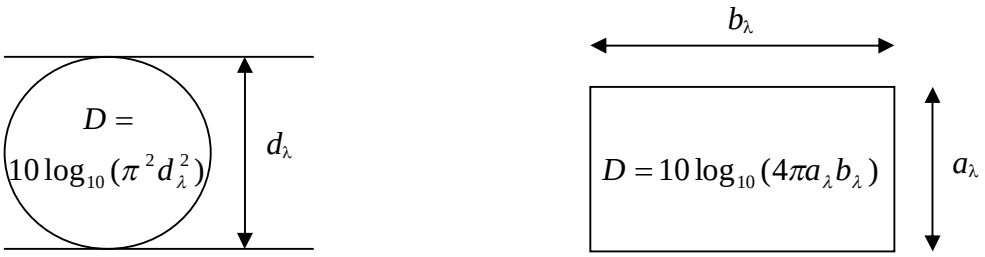

Figure 1 Directivity, D of circular and rectangular apertures expressed in dB over the equivalent isotropic case (i.e. dBi) [3]. The subscript λ indicates a dimension normalised to wavelength.

No.	Species	D(H) dBi	D(W) dBi	D(Rec) dBi	Measured dBi [2]	Frequency (kHz)	CF Range (kHz)
1	*Rhinolophus rouxii*	23.48	20.74	23.17	24	85	72-79
2	*Rhinolophus eloquens*	8.87	8.41	9.70	13	15	80-100
3	*Rhinolophus clivosus*	12.11	9.78	12.01	>10	25	70/100
4	*Rhinopoma hardwickei*	20.67	17.02	19.90	20	65	35
5	*Saccopteryx bilineata*	13.03	6.59	10.87	<10	45	45-50
6	*Rhynchonycteris naso*	18.56	13.03	16.86	11	105	105
7	*Asellia tridens*	25.96	24.09	26.09	20	135	111-124
8	*Cloeotis percivali*	20.55	21.96	22.31	20	165	212
9	*Hipposideros caffer*	10.43	12.01	12.28	18	35	145
10	*Hipposideros lankadiva*	20.91	19.06	21.04	30	45	70
11	*Otomops martiensseni*	12.84	7.57	11.27	12	14	13-15
12	*Tadarida brasiliensis*	19.97	16.45	19.27	12	70	45
13	*Tadarida macrotis*	23.14	12.94	19.10	15	55	21/35
14	*Tadarida pumila*	8.72	7.51	9.17	≤10	25	35-55
15	*Mormoops megalophylla*	4.28	2.62	4.51	20	20	50-60
16	*Pteronotus gymnonotus*	23.20	17.47	21.40	15	105	50-55
17	*Pteronotus parnellii*	23.71	17.16	21.50	16	95	60
18	*Pteronotus personatus*	19.04	14.72	17.94	<10	82	82
19	*Noctilio albiventris*	23.90	16.60	21.31	10	75	65-75
20	*Noctilio leporinus*	7.42	≈ 0	4.75	12	15	56-59
21	*Myotis evotis*	19.70	12.94	17.38	17	55	50-63

Table 1 Pinnae gain approximations produced by assuming a circular or rectangular aperture. Species selected form a subset of those reported in [2], and all have a significant CF component in their sonar emission.

It is not being claimed in this paper that the consideration of physical aperture alone is sufficient to understand the entire behaviour of the ear; on the contrary, it has already been shown that some bats have a frequency-independent directivity and in others there is clear inconsistency. Pinnae of the species *Macroderma gigas* and *Nyctophilus gouldi*, for example, have been much more accurately modelled by analogy to a radiating horn [4]. Nevertheless, there is some benefit in

classifying animals where the simple theory holds true in order to direct future research effort into those that do not, and which have potentially more interesting properties. Table 1 confirms that the rectangular aperture approximation has a reasonable agreement with the measured results, and this data is reproduced for visual comparison in Figure 2.

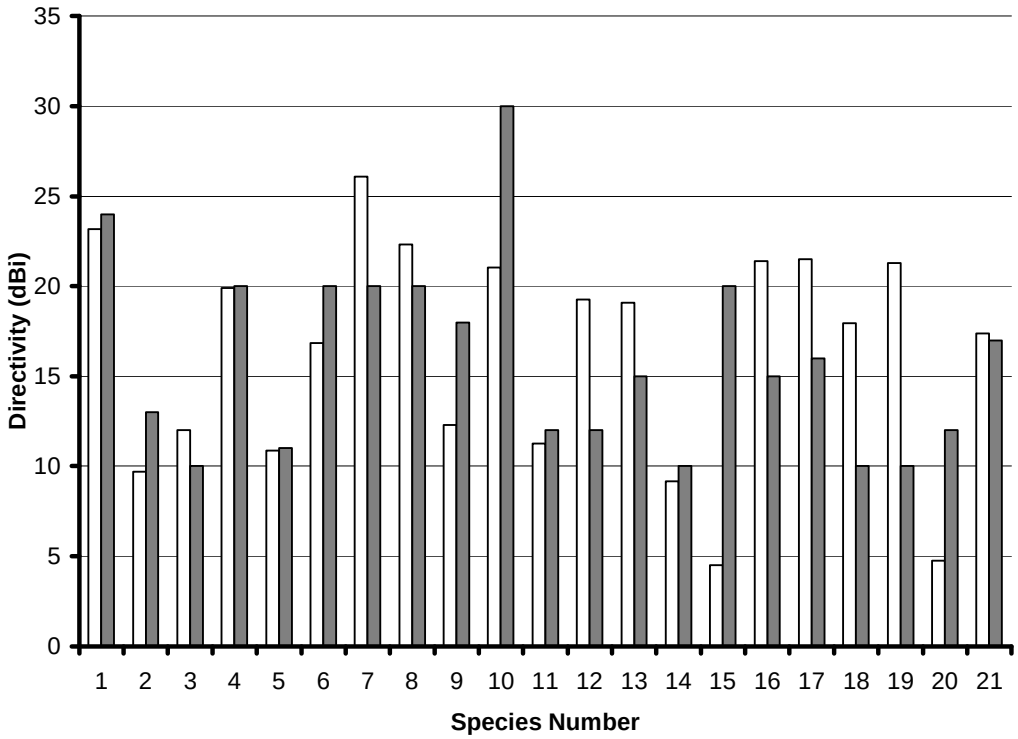

Figure 2 Graphical comparison between the directivity of a rectangular aperture (white bars) and the measured directivity (shaded bars) from [2]. The species numbering is as defined previously in Table 1.

One species where there is a good match is the Rufous Horseshoe bat (*Rhinolophus rouxii*). In order to further validate the simple model, and to examine the fine details of the directivity pattern of the pinna a full wave three dimensional modelling approach was undertaken. In this paper we will describe the method, validation and results of this modelling. In addition we will demonstrate good agreement between the simple model, measurements and the full field model for this particular species.

2. THREE DIMENSIONAL MODELLING

The Transmission Line Modelling (TLM) method is a time domain, differential numerical modelling technique ideally suited to the study of field problems [5]. It has found many applications including those within the field of bioacoustics [6, 7] and is broadly comparable with the finite difference method in the time domain [8]. TLM exploits the analogy between waves propagating in the acoustic field and pulses propagating on an orthogonal mesh of interconnected

transmission lines. These transmission lines are governed by differential equations which are isomorphic to those that of the transmission medium and thus the network can model the propagating waves. The equivalence of the transmission line model with the linearised Euler equations can be proved mathematically [9] and consequently it is possible to conceptually manipulate just the transmission lines. An additional advantage of applying transmission line equivalents is that stability criteria are guaranteed to be met when the model includes only passive electrical components. Typically TLM is applied to a structured arrangement of cubic or parallelepipedic cells ('the mesh') which are individually termed *nodes*. In this formulation, there is a direct mapping between nodes and the voxels in raw data sets available from medical scanning equipment.

2.1 Geometry preprocessing

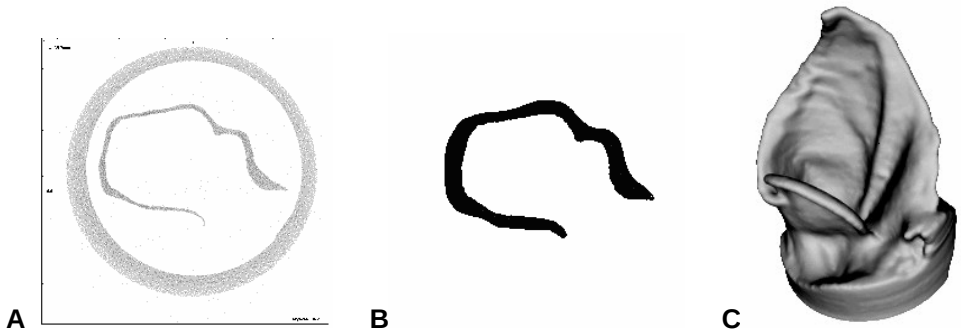

Figure 3 Preprocessing steps: (A) original CT data, (B) monochrome data, and (C) volume-rendered data [10].

The input data to the model was derived from original X-ray Computed Tomography (CT) data of the subject bat [10]. The data comprised of 256 slices in the z direction with a voxel size of 72 μm and a finer resolution within each slice of 18 μm in x and y. The images were processed to remove artefacts of the scan including the holder used to retain the specimen. In addition it was necessary to convert the voxels from a greyscale value to a monochrome value in order to generate a computational mask for the TLM simulation. The individual slice pre-processing and 3D rendered data set is illustrated inset in Figure 3. Down sampling was also required in order to reduce the resolution of the 3D data set; however care was taken to ensure that the final resolution met the dispersion requirements of the finite modelling technique, and also to ensure that fine geometrical features were not lost in the translation.

2.2 Numerical computation

A 3D scalar TLM node was first described in the field of electromagnetic TLM by Choi and Hoefer [11]. The TLM node is specified with six transmission line segments connected in a shunt (parallel) configuration. It can be shown that this node will also model acoustic wave propagation [7]. The 3D scalar node can be formulated to model spatial changes in the compressibility and equilibrium density of the material [12], however this capability is seldom required in airborne ultrasonics and the basic lossless node for homogeneous material is adequate in most cases. To carry out this work we have resampled the original data set to give cubic cells and then applied the basic 3D scalar node.

Actual calculations proceed via two distinct processes known as *scatter* and *connect*. Voltage impulses travelling along the mesh of transmission lines are *scatter*ed when they meet the transmission line junction within the node. The six voltage impulses impinging on the node junction (the *incident* voltages, denoted by a superscript *i* in the following expressions) are then reflected back towards the periphery of the cell (the *reflected* voltages, denoted by superscript *r*). Expressed mathematically in terms of a matrix operation,

$$ {}^{r}_{n}\mathbf{V} = \mathbf{S}\ {}^{i}_{n}\mathbf{V} \tag{1} $$

where n is the time step index, $\mathbf{V}$ is a voltage vector comprising of the 6 incident impulse magnitudes and $\mathbf{S}$ is defined thus:

$$ \mathbf{S} = \frac{1}{3}\begin{bmatrix} -2 & 1 & 1 & 1 & 1 & 1 \\ 1 & -2 & 1 & 1 & 1 & 1 \\ 1 & 1 & -2 & 1 & 1 & 1 \\ 1 & 1 & 1 & -2 & 1 & 1 \\ 1 & 1 & 1 & 1 & -2 & 1 \\ 1 & 1 & 1 & 1 & 1 & -2 \end{bmatrix} $$

This scattering process is normally viewed as a static process. The actual time marching in the algorithm is a consequence of the transit time of the pulses on transmission lines connecting adjacent nodes. Thus the second stage of the process, *connect*, is the process of exchanging reflected pulses between adjacent nodes such that they become new incident voltages, e.g.,

$$ {}^{i}_{n+1}V_{xp}(x,y,z) = {}^{r}_{n}V_{xn}(x+1,y,z) \tag{2} $$

where subscript xp indicates the node voltage on the transmission line aligned in the positive x direction and xn in the negative x direction. Both pressure and particle velocity can be imposed on and extracted from the mesh at each time step by observing certain equivalences, for example, in terms of the instantaneous pressure, P,

$$ P = \frac{1}{3}({}^{i}_{n}V_{xn} + {}^{i}_{n}V_{xp} + {}^{i}_{n}V_{yn} + {}^{i}_{n}V_{yp} + {}^{i}_{n}V_{zn} + {}^{i}_{n}V_{zp}) \tag{3} $$

In the model absorbing boundaries were applied on the periphery of the computational domain using a matched termination approach. The unconnected transmission lines are terminated during the connect process by applying a reflection coefficient of,

$$ \rho = \left(\frac{1-\sqrt{3}}{1+\sqrt{3}}\right) \tag{4} $$

which ensures that outgoing waves are absorbed. Internal boundaries were achieved by applying a reflection coefficient of +1 at the periphery of the solid regions being modelled. A more detailed explanation of the technique can be found in the cited literature [5–7, 9, 11, 12].

3. MODELLING METHOD VALIDATION

Prior to approaching the pinna model, tests were carried out on known benchmark problems to establish the validity. To facilitate the validation process it was necessary to transform the near field time domain data from the simulation to a frequency domain far field response.

3.1 Near to Far Field Transformation

Near-field to far-field transformations are required due to the physical limitations in computer memory and processing time. Often pressures are sampled in the near field and hence an extrapolation technique is needed to take these samples and project their effect in the far field. The method implemented in this paper is based on the integral equation of Kirchoff and Helmholtz and is similar to the approach adopted by Aroyan [8]:

$$p(\mathbf{R}) \approx \oint_S \left\{ jk.\hat{\mathbf{R}} \cdot \mathbf{n}.p(\boldsymbol{\sigma}) + \frac{\partial p(\boldsymbol{\sigma})}{\partial \mathbf{n}} \right\} e^{-jk\hat{\mathbf{R}}\cdot\boldsymbol{\sigma}} dS(\boldsymbol{\sigma}) \tag{5}$$

where k is the wave number ($= 2\pi/\lambda$), p is the complex pressure and all other parameters are as defined in Figure 4. The TLM model in conjunction with a Discrete Fourier Transform (DFT) is used to calculate the pressure and spatial derivatives on a surface surrounding the radiating object. This is often referred to an equivalent surface and is shown in Figure 4 labelled S. The key parameters to be captured on S during the simulation are the frequency domain pressure $p(\boldsymbol{\sigma})$ and the differential pressure with respect to the direction of $\boldsymbol{\sigma}$; $\frac{\partial p(\boldsymbol{\sigma})}{\partial \mathbf{n}}$. These are integrated numerically using a discrete version of Equation 5.

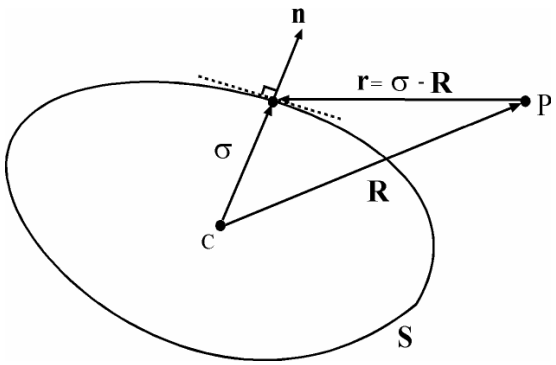

Figure 4 Near field to Far Field Transformation Arrangement

In the models analysed in this paper, it was convenient to select a cubic equivalent surface which surrounded the whole ear and center of rotation C. A cubic surface allows the nodes on the surface to be indexed in a simple 3D Cartesian coordinate system and simplifies the definition of vectors $\boldsymbol{R}$, $\boldsymbol{n}$ and $\boldsymbol{\sigma}$.

3.2 Benchmark simulations

Before implementing the ear geometry an identical simulation was run which incorporated identical boundary conditions and problem size. Point sources of pressure were excited within the mesh to verify correct operation as these have well-known analytical solutions for the field patterns generated. The calculated directivity patterns for bipole and tripole radiators with one

wavelength separation are shown in Figure 5. It can be seen that the agreement is reasonably good, however some variation is expected between analytical and numerical results as the analytical solutions is for infinitesimally small sources and in the TLM computation the sources are a finite size.

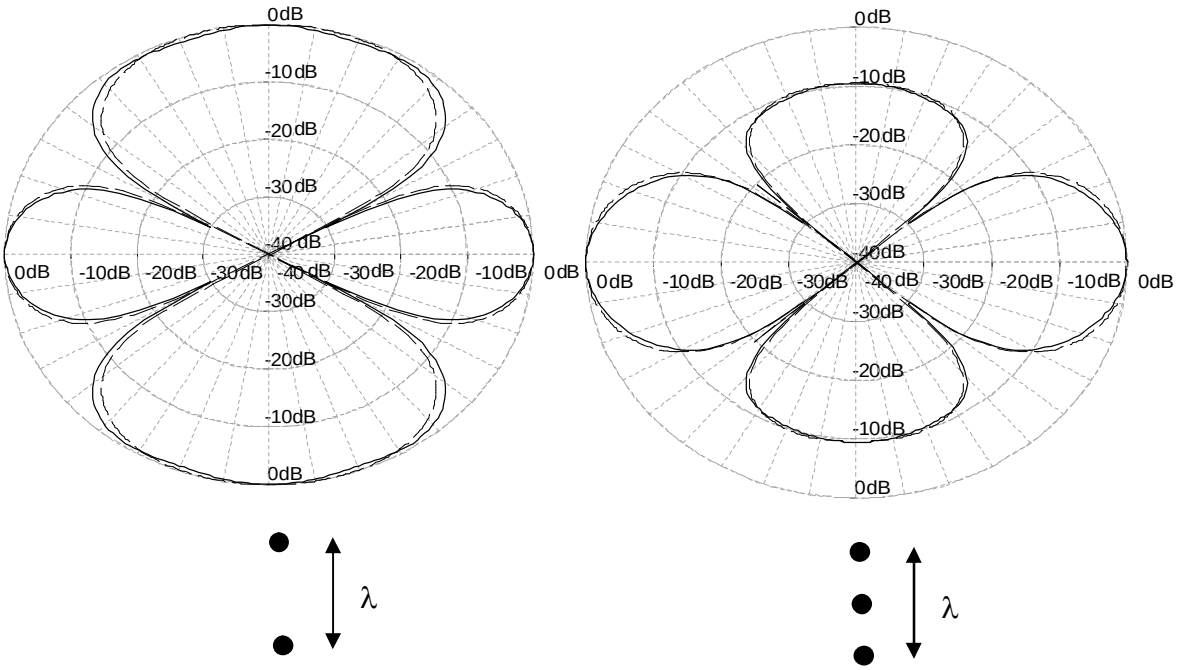

Figure 5 Far field directivity patterns for acoustic bipole and tripole radiators calculated using an exact analytical result (dashed line) and a TLM calculation (solid line).

This validation exercise provides an important reference for confirming the results of the simulation.

4. PINNA SIMULATION

The final simulations with ear geometry were carried out first with a sinusoidal excitation in the bat's CF emission band. Time domain output from this simulation is shown in Figure 6 (A). The base of the ear canal was closed in the simulation and the excitation was a point source placed in the centre of the cross-section. Further simulations were carried out using a broadband (impulsive) excitation and carrying out a DFT at the frequencies of interest. This data was transformed using the techniques already described to produce the directivity of the pinna in the far field. 2D projections of one of the 3D patterns generated by this approach are shown in Figure 6 (B) and (C). Note that the pinna images shown on the plots are merely to aid visualisation— the actual contour represents the normalised pressure magnitude that would be seen at a much larger range.

The directivity figure was calculated by taking the full far field pressure map and considering points where the pressure was ≥ -3 dB relative to the highest pressure value. From this a beam angle was estimated and the directivity value subsequently calculated. A full comparison of these results with those shown earlier is given in Table 2.

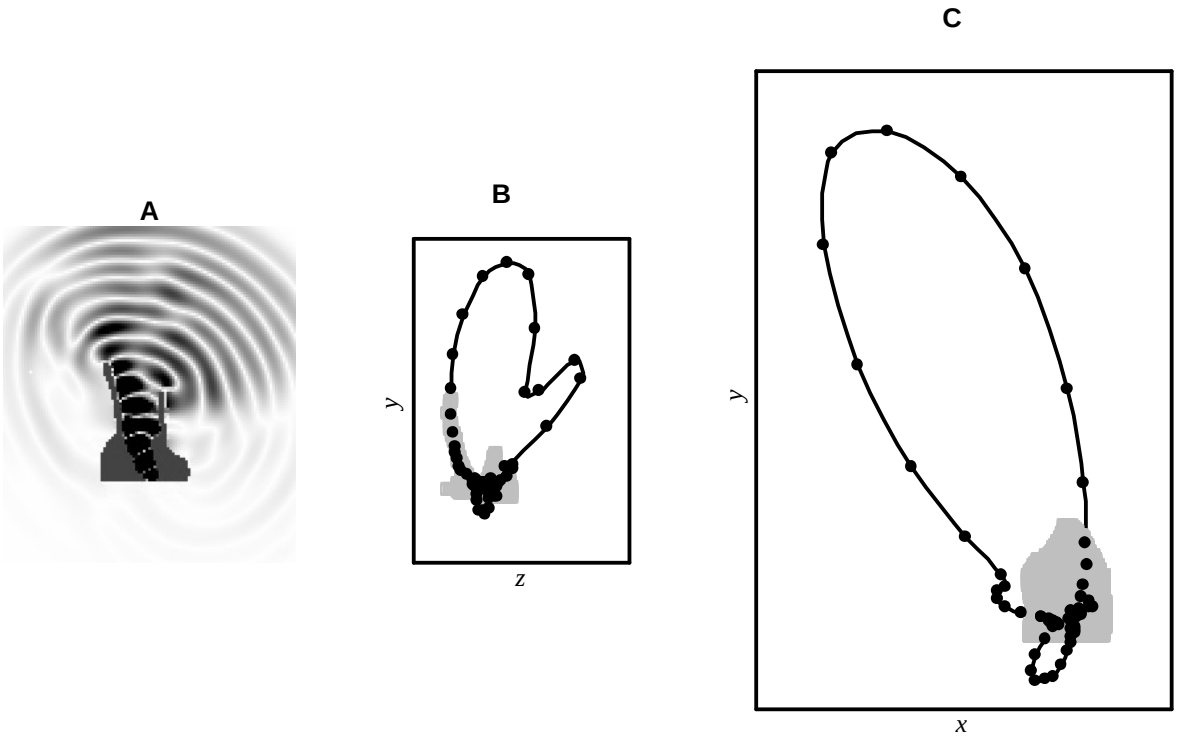

Figure 6 Simulation output for (A) a time domain snapshot of pressure (high pressure regions shaded grey), (B) and (C) the directivity pattern at the CF emission frequency (shown on a linear scale).

Origin of data	Directivity (dBi)
Measurement [2]	24
Rectangular aperture	23.17
TLM model	22.03

Table 2 Directivity estimates for *Rhinolophus Rouxii* pinna at 85 kHz.

The results seem to support the simple model of the pinna as an aperture at the frequency measured, which is near to the CF emission band.

5. CONCLUSION

In this paper we have considered hearing in the monaural case only, and have used the inverse problem of a radiating pinna to investigate its directional properties. It has been shown that the theory of a simple aperture has some value when comparing species. A numerical modelling method has been presented which gives good agreement with previously published measurements. Future work will focus on animals where the directivity appears higher than predictions, or where the shape of the pinna provides a frequency independent directivity.

6. ACKNOWLEDGEMENTS

The authors gratefully acknowledge The Royal Society and The European Union (IST Program, LPS Initiative, CIRCE Project IST-2001-35144) for financially supporting parts of this project.

REFERENCES

[1] Griffin D. R. Listening in the Dark. Yale U. P., New Haven 1958

[2] Obrist M. K., Fenton M. B. and Eger J.L. and Schlegel P.A. What ears do for bats: a comparative study of pinna sound pressure transformation in chiroptera. Journal of Experimental Biology. 1993. 180: 119-152.

[3] Kraus J. and Marhefka R. J. Antennas For All Applications. McGraw-Hill Education. 3rd Ed. 2001.

[4] Guppy A. and Coles R.P. Acoustical Aspects of Hearing and Echolocation in Bats. Animal Sonar: Processes and Performance. New York: Plenum Press. Edited by P. E. Nachtigall and P. W. B. Moore. 1988. 289-294.

[5] Johns P.B. and Beurle R.L. Numerical Solution of 2-Dimensional Scattering Problems using a Transmission-Line Matrix. Proceedings of the IEE 1971; 118:9: 1203-1208

[6] Goodson A. D., Flint J. A. and Cranford T.W. The Harbour Porpoise (Phocoena phocoena)-Modelling the Sonar Transmission Mechanism. Echolocation in Bats and Dolphins. Chicago. Edited by J. A. Thomas and C. F. Moss and M. Vater. 2004. 64-74

[7] El-Masri S., Pelorson X., Saguet P. and Badin P. Development of the Transmission Line Matrix Method in Acoustic Applications to Higher Modes in the Vocal Tract and other Complex Ducts. International Journal of Numerical Modelling: Electronic Networks, Devices and Fields. 1990. 3: 39-56.

[8] Aroyan J.L. Three- Dimensional Numerical Simulation of Biosonar Signal Emission and Reception in the Common Dolphin. PhD Dissertation, University of California, Santa Cruz, USA, 1996.

[9] Saleh A.H.M. and Blanchfield P. Analysis of acoustic radiation patterns of array transducers using the TLM Method. International Journal of Numerical Modelling: Electronic Networks, Devices and Fields. 1990. 3: 39-56.

[10] Müller, R. and Hallam J.C.T., Biomimetic Smart Antenna Shapes for Ultrasonic Sensors in Robots, Proceedings of the 35th International Symposium on Robotics ISR 2004.

[11] Choi D.H. and Hoefer W. J. R. The Simulation of Three-Dimensional Wave Propagation by a Scalar TLM model. MTT Symposium Digest, (San Francisco, CA, USA). IEEE. 1984. 70-71

[12] Porti J. A. and Morente J. A. A Three-Dimensional Symmetrical Condensed TLM Node for Acoustics. Journal of Sound and Vibration 2001, 241:2:207-222